Ground Motion Attenuation Model for Peak Horizontal Acceleration from Shallow Crustal Earthquakes

Vladimir Graizer,[a] M.EERI, and Erol Kalkan,[b] M.EERI

Spatial distribution of ground motion data of recent earthquakes unveiled some features of peak ground acceleration (PGA) attenuation with respect to closest distance to the fault (R) that current predictive models may not effectively capture. As such, PGA: (1) remains constant in the near-fault area, (2) may show an increase in amplitudes at a certain distance of about 3–10 km from the fault rupture, (3) attenuates with slope of R^{-1} and faster at farther distances, and (4) intensifies at certain distances due to basin effect (if basin is present). A new ground motion attenuation model is developed using a comprehensive set of ground motion data compiled from shallow crustal earthquakes. A novel feature of the predictive model is its new functional form structured on the transfer function of a single-degree-of-freedom oscillator whereby frequency square term is replaced with closest distance to the fault. We are proposing to fit ground motion amplitudes to a shape of a response function of a series (cascade) of filters, stacked separately one after another, instead of fitting an attenuation curve to a prescribed empirical expression. In this mathematical model each filter represents a separate physical effect. [DOI: 10.1193/1.2755949]

INTRODUCTION

Since the 1970s, peak ground motion attenuation relations have usually been represented by the logarithmic (10-base or natural) type of empirical equations (e.g., Trifunac 1976, Abrahamson and Silva 1997, Boore et al. 1997, Campbell 1997, Sadigh et al. 1997). According to Campbell (2003), "In its most fundamental form, an attenuation relation can be described by the following expression:

$$\ln Y = c_1 + c_2 M - c_3 \ln R - c_4 r + c_5 F + c_6 S + \varepsilon \tag{1}$$

where Y is the strong-motion parameter of interest, M is the earthquake magnitude, r is a measure of source-to-site distance, F is a parameter characterizing style of faulting, S is a parameter characterizing the type of local site conditions, ε is a random error term with zero mean, and R is a distance term." The logarithmic equation form has been used because ground motion data are generally log-normally distributed. One advantage of this representation is the ability to model standard deviation (σ) in logarithmic space, which turns σ into a constant amplifier/deamplifier in the arithmetic space.

[a] California Geological Survey, Sacramento 95814; E-mail: vgraizer@consrv.ca.gov
[b] California Geological Survey, Sacramento 95814; E-mail: Erol.Kalkan@conservation.ca.gov

Earthquake Spectra, Volume 23, No. 3, pages 585–613, August 2007;

With collection of more strong-motion data, attenuation relationships have become more complicated (incorporating a number of additional parameters, which are determined with significant error) and usually difficult to implement by their users (PEER 2006). The common features of these models are the slower attenuation they yield in the vicinity of fault zone with a smooth turning point at a distance of a few kilometers apart from the fault and faster attenuation at farther distances. On the other hand, it is not always easy to assess the physical meaning of all parameters included in recent predictive relations since they mostly have addition and subtraction of a series of entities or embedded logarithmic functions into the main logarithmic equation form. Another potential limitation can come from accounting for saturation of ground motion with large magnitudes (a notion commonly accepted among developers of the next generation of attenuations [NGA]; PEER 2006) since it requires the whole attenuation curve to be relatively low not only at short but also at intermediate fault distances. The presently used form of attenuation expressions puts constraints on the shape of an attenuation curve by predicting exponential and R^{-n}-type decay with distance.

The primary questions that need to be addressed regarding the current relationships are:

- Do they effectively reflect current knowledge on the physical phenomena?
- Is it possible to develop an attenuation relationship that, while being in better consistency with recent findings in strong-motion seismology, still retains a simple physical interpretation?

Spatial distribution of ground motion data recorded in the proximity of the earthquake fault zones (2004 Parkfield, 1979 Imperial Valley, 1999 Chi-Chi, 1989 Loma Prieta, and 1994 Northridge) revealed important attenuation characteristics of peak ground acceleration (PGA) with respect to distance from the source as such: PGA (1) remains constant in the near-fault area, (2) exhibits a bump (an increase in amplitude) or a turning point at certain distance (about 3–10 km) from the fault surface, (3) attenuates with slope of R^{-1} and faster at larger distances, and (4) has amplitudes that can be amplified at certain distances as a result of basin effect. The well-known transfer function of a single-degree-of-freedom (SDOF) oscillator has analogous characteristics such that it remains constant at low frequencies (f), attenuates proportionally to f^{-2} at high frequencies, and may have a resonance (bump) around the natural frequency, f_0, depending upon damping, D_0. Based on this analogy, a conceptual approach is suggested in this paper in which ground motion parameters are treated as an output of cascading filters (with distance R being equivalent to square of frequency, f^2), whereby each filter is a mathematical expression used to simulate a certain physical phenomenon. Accordingly, the first filter has a response characteristic with constant level at very short fault distances, a bump or a turning point around R_0 (depending upon magnitude), and a decrease proportional to R^{-1}. The second filter can have two different settings. The first exhibits a constant level till R_1 (around 100 km from the fault) with damping $D_1=0.65$ (no bump) and a decrease proportional to $R^{-0.5}$. The second setting has lower damping with $D_1 \sim 0.40$. Utilizing a second filter with parameter $D_1=0.65$ essentially does not affect attenuation of PGA at distances shorter than R_1, and results in faster attenuation $R^{-1.5}$ at distances more than the threshold distance R_1. By varying the damping parameter, this secondary

filter can also successfully capture basin effect by slightly amplifying ground motions in the near field and more at distances around R_1. These settings also result in faster attenuation $R^{-1.5}$ at distances more than the threshold distance R_1. Similar to the basin effect, this filter can be tuned to model a possible bump on the attenuation curve due to reflection from Moho surface at distances of about 50–60 km from the source (Somerville and Yoshimura 1990). It should be noted that this intermediate distance filter is aimed to be included in attenuation modeling only when the data do sample a deep basin, so that a specific set of observations is actually biased by this effect. In this study, style of faulting is considered as a simple scale factor. Parameter R_0 (we will also refer to it as corner distance) is found to be a linear function of magnitude increasing from 3 km for M_W 4.5 to about 10 km for M_W 8.0. It is also shown that parameter D_0 has significant effects on attenuation curve by quantifying the intensity of bump. Initial findings demonstrate that it is a function of magnitude reaching minimum with $D_0=0.4$ (producing a significant bump) for $M_W \sim 6.0-6.5$. D_0 becomes larger at $M_W < 5.0$ and $M_W > 7.0$ (either no or low-level increase of peak amplitude at distance R_0 from the fault).

It should be emphasized that seismic waves attenuate and change their amplitude in space and time as they propagate. These dynamic changes are direct consequences of reflection, geometric spreading, scattering, multipathing, and other phenomena. These complicated processes are in a way "natural filtering" of wave amplitudes. Thus, our approach of using cascading filters in attenuation modeling takes its spirit from this natural process. Their functional forms were constructed using an analogy between frequency square and distance, which allows us to apply a classical approach used in signal processing where the function of a filter is to remove or extract part of the signal. Similarly, each filter acts independently at different distances. One can also look at this approach as a mathematical combination of distance-dependent cascading functional forms. The novel feature of this approach is its inherent versatility, as such future modifications (or refinements) on each filter can be achieved independently without changing the settings of other filters. The developed model uses moment magnitude M_W as a magnitude measure (henceforth referred to simply as "M"), and closest distance to the fault (referred to as "fault distance") as a distance measure. It is structured on the NGA database (Power et al. 2006) with a number of additions mainly from recent California earthquakes. Specifically, almost two-thirds of data utilized in this study comes from the NGA data set.

The developed model is not only theoretically robust and original, but also practically yields good predictive performance against the actual data recorded at a broad range of magnitude levels within a wide range of distances. In contrast to recent attenuation relationships, it provides ease in both implementation and interpretation of its equation form as well as its physical parameters while providing comparable standard deviation. The model includes amplification due to reduction in soil stiffness by incorporating shear-wave velocity in the upper 30 m as an independent variable. To account for deep geological structure response, "basin effect," a new parameter is introduced. Basin-effect correction significantly improved the predictive power of the model against, for instance, Hector Mine and Landers earthquake data.

GROUND MOTION DATABASE

In this study, a total of 2,583 data points from 47 worldwide shallow crustal earthquakes with focal depths less than 20 km were utilized. All earthquakes occurred in the shallow crustal tectonic regime considered to be similar to that of California. Table 1 presents these events with relevant information on their moment magnitude, focal depth, epicenter coordinates, and fault mechanism. Also listed is the breakdown of record numbers used from each event. Of the total 2,583 records, 1,450 records are from reverse events, 1,120 from strike-slip events, and 13 are from normal fault events. In addition to the events gathered from the Pacific Earthquake Engineering Research Center database created under the NGA project, Table 1 also includes a number of additional events or data from additional stations for the events in the NGA data set. The 1994 Northridge, 1999 Hector Mine (Graizer et al. 2002), 2002 Big Bear City, 2003 San Simeon, 2004 Parkfield, 2005 Anza and Yucaipa, 1976 Gazli (Uzbekistan, former USSR), 1988 Spitak (Armenia, former USSR), and 1991 Racha (Georgia, former USSR) strong-motion data were compiled by the first author, while the 1999 Kocaeli, Duzce, and other Turkish earthquake data were incorporated by the second author (Kalkan and Gulkan 2004). For example, the Hector Mine data set used in our study includes 213 data points compared to 84 used in the NGA database, and the Northridge earthquake subset was also enriched by including a number of PGA values recorded at relatively large distance stations.

The distributions of earthquake data with respect to moment magnitude and PGA plot against fault distance are shown in Figure 1. As seen, the compiled data set becomes more complete with refined additions to the existing NGA database not only at farther distances but also in the near-field region; it is also more inclusive in terms of magnitude range covered. The current set includes data recorded within 250 km of the earthquake faults from events in the magnitude range of 4.9 to 7.9. The latest entries are the Anza and Yucaipa earthquakes of 12 and 16 June 2005. The data used in the analysis represent main shocks only; hence records from any aftershocks within the NGA data set were excluded. The widely accepted method of reflecting the effects of geological conditions on the ground motion is to classify the recording stations according to their average shear-wave velocity in the upper 30 m (V_{S30}; Boore et al. 1997). Figure 2 plots the distribution of earthquake data with respect to V_{S30} measurement at each station. Also shown as a reference is the NEHRP site categorization. It should be noted that approximately half of the stations in our database have measured shear-wave velocity profiles, while the rest do not.

ATTENUATION-MODEL DEVELOPMENT

The attenuation model developed here is limited to distances where ground motions may have significant intensity for engineering applications. We realize the scientific importance of attenuation of ground motions at distances larger than 250 km and for PGAs below 0.005 g (the common triggering level of strong-motion instruments). But extending attenuation predictions to larger distances requires combining data from triggered instruments and continuous recording stations. This issue requires special study and is

Table 1. List of events used in development of attenuation relationship

No.	Event	Date	Style of Faulting	M_w	Depth (km)	Epicenter Coordinates		Number of Data	Distance Range (km)	Data Source*
						Latitude	Longitude			
1	ADANA-CEYHAN (TURKEY)	1998	Strike-Slip	6.3	18.0	36.850	35.550	4	28.0 – 96.0	3
2	ANZA	2005	Strike-Slip	5.2	14.2	33.529	−116.573	279	4.8 – 197.6	2
3	BIG BEAR CITY	2003	Strike-Slip	5.2	6.3	34.310	−116.848	178	8.6 – 166.7	1
4	BINGOL (TURKEY)	2003	Strike-Slip	6.4	6.0	38.940	40.510	1	6.1	3
5	BISHOP (RND. VAL.)	1984	Strike-Slip	5.8	9.0	37.460	−118.590	1	21.9	1
6	BORREGO MNT.	1968	Strike-Slip	6.6	8.0	33.190	−116.142	5	45.7 – 222.4	1
7	CHALFANT VALLEY	1986	Strike-Slip	5.8	6.7	37.577	−118.449	5	6.4 – 24.5	1
8	CHI-CHI (TAIWAN)	1999	Reverse	7.6	16.0	23.860	120.800	420	0.3 – 172.2	1
9	COALINGA-01	1983	Reverse	6.4	4.6	36.233	−120.310	46	8.4 – 55.8	1
10	COALINGA-05	1983	Reverse	5.8	7.4	36.241	77.191	11	4.6 – 16.2	1
11	COYOTE LAKE	1979	Strike-Slip	5.7	9.6	37.085	−121.505	10	3.1 – 33.8	1
12	DENALI (ALASKA)	2002	Strike-Slip	7.9	4.9	63.538	−147.444	24	2.7 – 275.9	1
13	DINAR (TURKEY)	1995	Normal	6.4	5.0	38.110	30.050	2	3.0 – 39.6	3
14	DÜZCE (TURKEY)	1999	Strike-Slip	7.2	10.0	40.740	31.210	23	0.2 – 188.7	3
15	ERZİNCAN (TURKEY)	1992	Strike-Slip	6.9	9.0	39.720	39.630	2	5.0 – 65.0	3
16	FRIULI (ITALY)	1976	Reverse	6.5	5.1	46.345	13.240	5	15.8 – 102.2	1
17	GAZLI (UZBEKISTAN)	1976	Reverse	6.8	10.0	40.381	63.472	1	5.0	2
18	RACHA (GEORGIA, USSR)	1991	Reverse	6.2	9.0	42.461	44.009	8	37.0 – 155.0	2
19	GULF OF CALIFORNIA	2001	Strike-Slip	5.7	10.0	32.037	−114.906	12	76.7 – 134.1	1
20	HECTOR MINE	1999	Strike-Slip	7.1	5.0	34.574	−116.291	213	10.7 – 259.3	2
21	IMPERIAL VALLEY	1979	Strike-slip	6.5	10.0	32.644	−115.309	33	0.1 – 50.1	1
22	KOCAELI (TURKEY)	1999	Strike-Slip	7.4	15.0	40.727	29.990	31	3.2 – 349.6	3

Table 1. (cont.)

No.	Event	Date	Style of Faulting	M_w	Depth (km)	Epicenter Coordinates		Number of Data	Distance Range (km)	Data Source*
						Latitude	Longitude			
23	LANDERS	1992	Strike-Slip	7.3	7.0	34.200	−116.430	69	2.2 – 190.1	1
24	LAZIO-ABRUZZO (ITALY)	1984	Normal	5.8	14.0	41.710	13.902	5	18.9 – 51.3	1
25	LITTLE SKULL MTN. (NEVADA)	1992	Normal	5.7	12.0	36.720	−116.286	8	16.1 – 100.2	1
26	LIVERMORE	1980	Strike-Slip	5.8	12.0	37.855	−121.816	7	16.7 – 56.1	1
27	LOMA PRIETA	1989	Reverse/ Strike	6.9	17.5	37.041	−121.883	82	3.9 – 117.1	1
28	MAMMOTH LAKES-02	1980	Strike-Slip	5.7	14.0	37.628	−118.927	3	9.1 – 16.9	1
29	MAMMOTH LAKES-03	1980	Strike-Slip	5.9	16.0	37.561	−118.831	4	5.9 – 11.5	1
30	MAMMOTH LAKES-04	1980	Strike-Slip	5.7	5.0	37.625	−118.859	4	2.8 – 14.2	1
31	MAMMOTH LAKES-06	1980	Strike-Slip	5.9	14.0	37.506	−118.856	5	12.0 – 46.5	1
32	MANJIL (IRAN)	1990	Strike-Slip	7.4	19.0	36.810	49.353	7	12.6 – 174.6	1
33	MORGAN HILL	1984	Strike-Slip	6.2	8.5	37.306	−121.695	28	0.5 – 70.9	1
34	NORTHRIDGE	1994	Reverse	6.7	17.5	34.206	−118.554	174	4.0 – 78.1	2
35	NORTH PALM SPRINGS	1986	Strike-Slip/ Thrust	6.1	11.0	34.000	−116.612	32	8.6 – 268.0	1
36	PARKFIELD	1966	Strike-Slip	6.2	10.0	35.955	−120.498	6	6.3 – 63.3	2
37	PARKFIELD	2004	Strike-Slip	6.0	8.8	35.819	−120.364	94	0.3 – 169.6	2
38	SAN FERNANDO	1971	Reverse	6.6	13.0	34.440	−118.410	44	1.8 – 218.8	1
39	SAN SIMEON	2002	Reverse	6.5	7.1	35.702	−121.108	138	12.4 – 317.8	1
40	SANTA BARBARA	1978	Thrust	5.9	12.7	34.399	−119.681	2	12.2 – 27.4	1
41	SIERRA MADRE	1991	Reverse	5.6	12.0	34.259	−118.001	9	10.4 – 48.2	1
42	SPITAK (ARMENIA)	1988	Reverse	6.8	5.0	40.987	44.185	1	25.0	2

Table 1. (cont.)

No.	Event	Date	Style of Faulting	M_w	Depth (km)	Epicenter Coordinates		Number of Data	Distance Range (km)	Data Source*
						Latitude	Longitude			
43	SUPERSTITION HILLS-02	1987	Strike-Slip	6.5	9.0	33.022	−115.831	11	1.0 – 27.0	1
44	TAIWAN, SMART(5)	1981	Reverse	5.9	11.1	24.429	121.896	7	28.7 – 32.0	1
45	WHITTIER NARROWS	1987	Reverse	6.0	14.6	34.049	−118.081	116	14.5 – 103.9	1
46	YOUNTVILLE	2000	Strike-Slip	5.0	10.1	38.379	−122.413	25	9.9 – 95.7	1
47	YUCAIPA	2005	Reverse	4.9	11.6	34.058	−117.011	388	2.6 – 160.1	2
							Total =	2,583		

* Data compiled by: (1) NGA; (2) V. Graizer; (3) E. Kalkan.

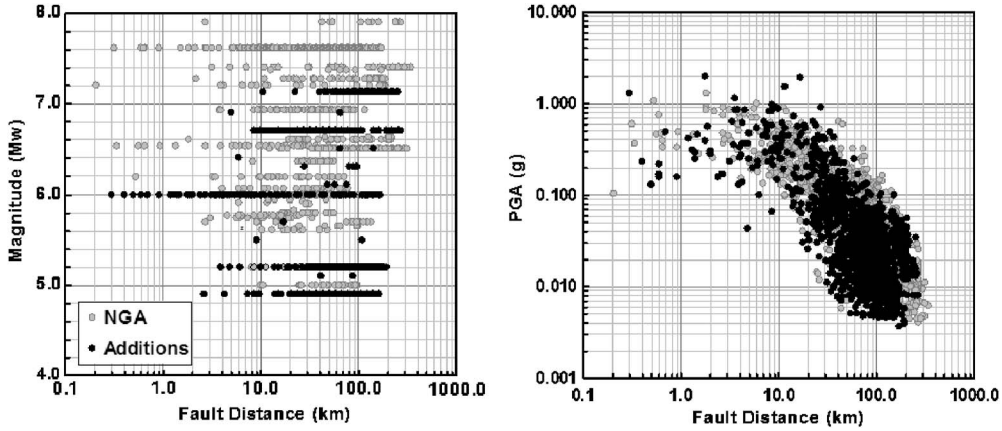

Figure 1. Earthquake data distribution with respect to moment magnitude (left) and PGA (right).

beyond the scope of this paper. On the other hand, the suggested approach can be easily applied to the data recorded at distances of more than 250 km by including an additional filter (explained in detail later).

Despite new strong-motion data recorded from a number of recent large and moderate earthquakes, there are still not sufficient data recorded in the close proximity of earthquake faults that can uniquely prove certain hypotheses about behavior of strong-motion attenuation function in the near field (0 to 5 km from fault rupture). It is especially true for large earthquakes with magnitudes larger than 7.0. Unfortunately, it is typical to have one near-fault strong-motion measurement, as in the cases of the 2002 M7.9 Denali or 1999 M7.1 Hector Mine earthquakes. The M6.0 Parkfield earthquake of 2004, however, represents a rare case of good near-source coverage. This event was recorded with a large number of near-field instruments deployed in a series of mostly fault-normal arrays. The Parkfield distribution of PGA with distance clearly demonstrates that the largest accelerations were not recorded at the stations closest to the fault (Shakal et al. 2005). Similar observations can be also made about 1999 M7.6 Chi-Chi and the 1979 M6.5 Imperial Valley earthquakes.

The question is whether it is an anomaly or a universal feature. The answer may depend on the distribution of fault slip on the fault surface. We are planning to conduct ground motion–modeling studies to examine the distance dependence in the real vicinity of the fault at distances much smaller than the rupture length. For example, the solution for residual displacements from a buried dislocation shown in a classical paper by Chinnery (1961) demonstrates an important pattern, as such residual displacements near the edges of the dislocation attenuate slower than those in the middle of the fault. Another possible reason for the effect of relative increase of amplitudes (i.e., focusing) may be a change in predominant type of seismic radiation at different distances (Haskell 1969). Accordingly, an observer located at the fault surface is subjected to only step-type mo-

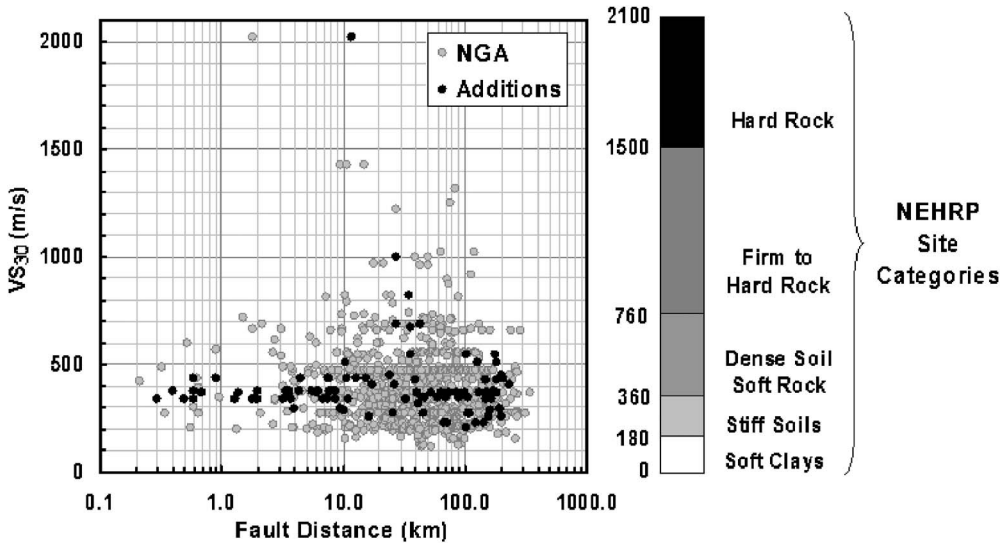

Figure 2. Earthquake data distribution with respect to V_{S30} and its comparison with NEHRP site categories.

tion (residual displacement), but moving slightly away from the fault makes the effect of *S*-wave become significant (even one cannot separate residuals from body waves at close distances). In a more realistic case of complex slip distribution with ups and downs along the fault surface, maximum values of PGA will be recorded near the maximum slip on the fault. With random distribution of a limited number of stations in the vicinity of a long fault rupture, maximum values of PGAs may not necessarily occur at the closest stations. In a way, a bump in attenuation is likely the result of a number of effects, such as elongated fault, edge effects, directivity, and obviously geologic and topographic structure. Partially, it is also a result of measuring distance from the closest part of the fault (so far there is no good distance measure for distances less than the fault length). Simulating earthquake strong ground motions using recordings of small earthquakes for different distribution of fault slip and asperities can also be helpful in understanding this phenomenon (Frankel 1995).

Nevertheless the currently used attenuation relationships are not accounting for these near-fault characteristics, primarily due to the lack of sufficient near-fault data available at the time of their development. In fact, within a window of less than 10 years, the near-fault ground motion database was significantly enriched and could change the common perspective, which has long been structured based on data recorded at farther distances.

The recent earthquakes that occurred in California, Taiwan, and Turkey not only increased the number of recorded data in the near fault, but also generated a large amount of data beyond 20 km of the fault rupture. Attempts to fit into this extensive yet sparse data set in a purely empirical fashion results in more complicated attenuation relation-

ships (not only in terms of an equation form but also in terms of introduction of additional parameters related to fault, source, or soil characteristics) without strong physical reasoning. Although the objective is always to have better yet consistent predictions, introducing new but not well-determined parameters inevitably increases the epistemic uncertainties. However, recent earthquakes (e.g., 2004 Parkfield, 1979 Imperial Valley, 1999 Chi-Chi, 1989 Loma Prieta, and 1994 Northridge) reveal important physical evidence on the attenuation of PGA in the near-fault zone that many attenuation relations fail to represent. The observed attenuation characteristics of PGA with respect to distance during these earthquakes are listed below:

- A constant level in the area closest to the fault rupture.
- A slope of about R^{-1} at distances of more than 10 km and $R^{-1.5}$ (i.e., faster) at farther distances.
- Possibly, a bump at a distance of about 3 – 10 km from the fault rupture.

Primary motivation of this study is therefore to develop a new predictive model, the architecture of which is set on our physical/mechanical knowledge on the attenuation of seismic radiation rather than on a purely empirical basis. This model should be able to replicate the observed near-fault attenuation of acceleration, be theoretically robust, and retain the simplicity for its interpretation by the user. Its parameters should have clear physical meaning, be measurable with reasonable accuracy, and be absolutely necessary for providing reliable attenuation.

DEVELOPMENT STAGES

The following criteria are set in the development of a new attenuation relationship:

- Amplitude of ground motion is constant and not decreasing in the near field.
- Amplitude of ground motion can amplify with increasing distance to the fault in the real proximity of the fault rupture, at distances much less than the length of the fault rupture.
- At farther fault distances (more than 10 km), PGA attenuates with R^{-1}, and faster (such as $R^{-1.5}$) at distances more than 100 km.

Functions demonstrating similar behavior are well known in physics. The transfer function of a SDOF oscillator exhibits analogous characteristics in such a way that it:

- Has a constant level at low frequencies.
- Attenuates proportionally to f^{-2}.
- May have a bump or a turning point depending upon damping, D_0.

Accordingly, the well-known transfer function of a SDOF oscillator can be written as:

$$G(\lambda) = \frac{A}{\sqrt{(1-\lambda^2)^2 + 4D_0^2\lambda^2}} \tag{2}$$

where $\lambda = \omega/\omega_0$, A is the amplification coefficient (i.e., scaling parameter of functional shape), ω is cyclic frequency, and ω_0 is natural cyclic frequency.

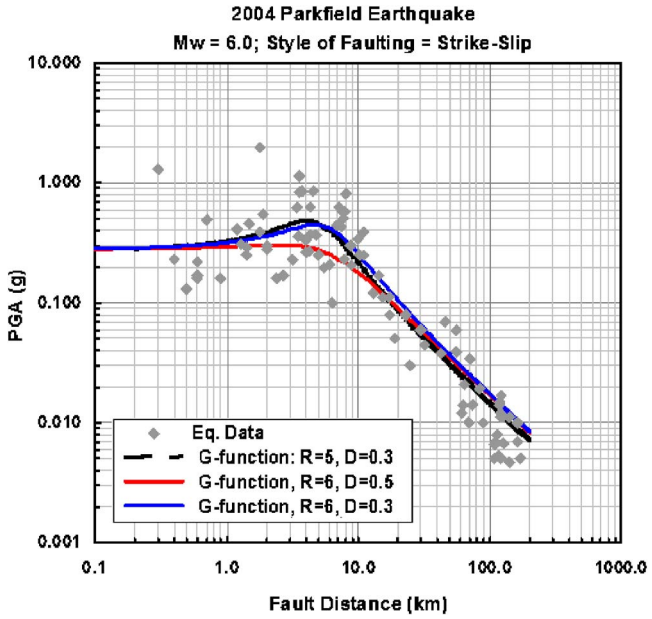

Figure 3. 2004 Parkfield earthquake PGA data and attenuation plots of *G*-functions with various *R* and *D*.

It is important to note that the analogy made between distance decay of PGA and SDOF oscillator transfer function is functional rather than physical. SDOF transfer function provides unique shape features that are needed to describe the observed decay of ground motion. We are proposing to fit ground motion amplitudes to a shape of a response function of cascading filters, stacked separately one after another, instead of fitting an attenuation curve to a prescribed empirical expression. In this mathematical model each filter represents separate physical effect.

This representation resembles the digital signal processing and allows creation of a system with desired response. The resultant response in fact is a multiplication of transfer functions of each individual filter accounting for different effects in the arithmetic space.

According to this analogy, distance R, when structured between SDOF transfer function and attenuation of acceleration, can replace square of frequency f^2 in Equation 2. Replacing ω^2 with R, and ω_0^2 with R_0 yields:

$$G(R) = \frac{A}{\sqrt{\left(1 - \frac{R}{R_0}\right)^2 + 4D_0^2 \frac{R}{R_0}}}. \tag{3}$$

Figure 3 demonstrates comparison of outputs of Equation 3 against the Parkfield earth-

quake data using the following three sets of parameters:

$$\text{Case 1: } R_0 = 5 \text{ km}, \quad D_0 = 0.3, \quad A = 0.28$$

$$\text{Case 2: } R_0 = 6 \text{ km}, \quad D_0 = 0.3, \quad A = 0.28$$

$$\text{Case 3: } R_0 = 6 \text{ km}, \quad D_0 = 0.5, \quad A = 0.28.$$

As seen, increasing R_0 shifts the bump to larger distances, while increasing damping D_0 to about 0.65 removes the bump (this is well known to instrument developers).

By allowing ground motion parameters as outputs of a series of filters (if one assumes $G(R)$ as a filter function for ground response), the proposed approach is extremely versatile. For instance, it is possible to increase the slope of attenuation at farther distances by adding a secondary filter with parameters set to yield a flat amplification of 1.0 (no amplification) till for instance, a distance of 100 km, and a slope of $R^{-0.5}$ at greater distances. Mathematically, this secondary filter can be obtained by slight modification of Equation 3 as such (replacing ω^4 with R, and ω_0^4 with R_1):

$$G_1(R) = \frac{A}{\sqrt{\left(1 - \sqrt{\frac{R}{R_1}}\right)^2 + 4D_1^2\sqrt{\frac{R}{R_1}}}} \tag{4}$$

where R_1 is the distance threshold after which faster attenuation takes place and D_1 is 0.65–0.7 (this set-up will produce smooth transition to the faster attenuation at distances larger than R_1). If parameterized accordingly (e.g., $R_1 = 60$ km and $D_1 = 0.5$), this filter can capture a possible bump on the attenuation curve due to reflection from Moho surface at distances of about 50–60 km from the source (Somerville and Yoshimura 1990).

Figure 4 demonstrates the implementation of faster attenuation via the secondary filter described by Equation 4 to the Parkfield data. The parameters of Equation 4 were set to: $D_1 = 0.7$, and $R_1 = 100$ km. Therefore the final slope of the attenuation function of $G \times G_1$ at distances of more than 100 km increases to $R^{-1.5}$.

In natural logarithmic space the attenuation formula corresponding to plots in Figure 4 can be written as:

$$\ln Y = \ln G(R) + \ln G_1(R) \tag{5}$$

Or, it can be expanded into the following form:

$$In(Y) = In(A) - 0.5In\left[\left(1 - \frac{R}{R_0}\right)^2 + 4D_0^2\frac{R}{R_0}\right] - 0.5In\left[\left(1 - \sqrt{\frac{R}{R_1}}\right)^2 + 4D_1^2\sqrt{\frac{R}{R_1}}\right] + \sigma_{InY} \tag{6}$$

where σ_{InY} is the total standard deviation of the equation. Each estimator parameter (i.e., A [amplification coefficient], D_0, R_0, and D_1, R_1) in Equation 6 is detailed next to satisfy the following attenuation characteristics of PGA:

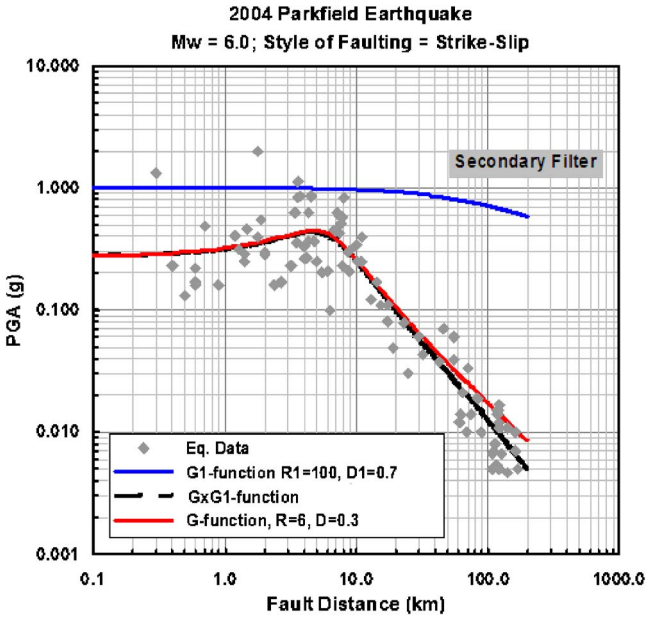

Figure 4. 2004 Parkfield earthquake PGA data and implementation of a secondary filter to the primary attenuation function (i.e., $G \times G_1$ function fit).

- For magnitudes less than about 5.0 there is no bump. Amplitude of PGA decreases starting from the corner distance, R_0 (analog to corner frequency).
- For magnitudes larger than 5.0 maximum value of PGA takes place not necessarily on the fault, but at a certain (corner) distance. We expect this focusing phenomenon to happen at distances varying from 3 to 10 km.
- There is a saturation of the average PGA with magnitude, probably around magnitude 7.0 or 7.5.

As of today there is still not enough recorded data in the near field to allow a unique decision about the shape of the attenuation curve. Seemingly, there are only few complete data sets that have at least a dozen data points in the near-fault zone (e.g., M6.0 Parkfield, M7.6 Chi-Chi, M6.7 Northridge, M6.5 Imperial Valley).

PHYSICAL INTERPRETATION OF R_0 AND D_0

For the SDOF oscillator, f_0 refers to the natural frequency. In our attenuation formulation, it corresponds to a corner distance (R_0) where the highest ground motion (bump) or a turning point is observed. By the same analogy, the corner distance can be referred to corner frequency. R_0 is clearly a function of earthquake magnitude. Based on earthquake data utilized, Figure 5 (left panel) exhibits a linear function of magnitude with change in corner distance R_0. This relation is expressed as:

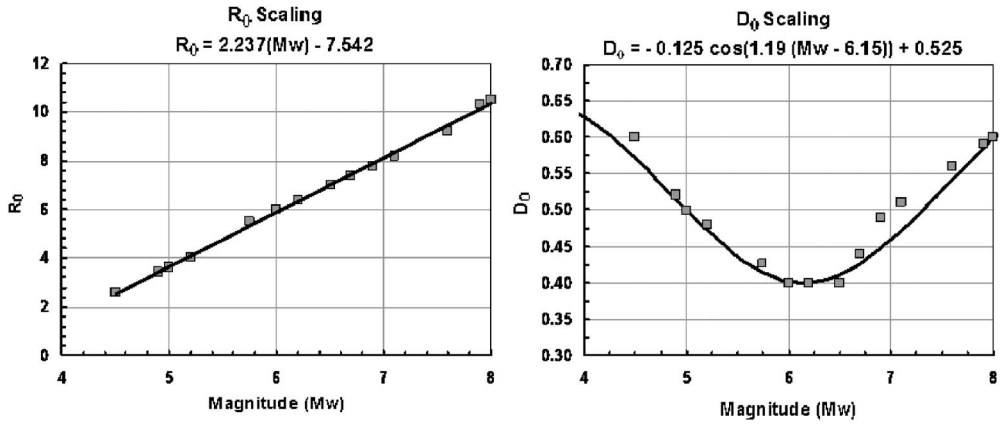

Figure 5. D_0 and R_0 scaling with magnitude.

$$R_0 = c_4 M + c_5 \tag{7}$$

where c_4 and c_5 are the estimator coefficients. Equation 7 implies that for larger magnitudes, turning point on attenuation curve occurs at farther distances. A certain analogy can also be seen between corner distance and the corner frequency in Brune's model (1970, 1971), where corner frequency depends upon the size of the earthquake.

D_0 is another important parameter and quantifies the intensity of the bump on the attenuation curve. Initial findings demonstrate that it is a function of magnitude reaching minimum with $D_0 = 0.4$ (producing a significant bump) for M6.0–6.5 and being higher at $M < 5.0$ and $M > 7.0$ (much lower or no bump). Equation 8 represents its magnitude dependency, while its variation with respect to magnitude is manifested in Figure 5 (right panel).

$$D_0 = c_6 \cos(c_7 M + c_8) + c_9. \tag{8}$$

In Equation 8, c_6, c_7, c_8, and c_9 are again the estimator coefficients. Equation 8 reaches minimum of about 0.4 for magnitudes 6.0 to 6.5 and generates a significant bump on the attenuation curve. Whether these trends are genuine cannot be answered until further investigation based on more data recorded in the near-fault regions is conducted. Relative level of the bump decreases for larger and smaller magnitudes. For magnitudes larger than 7.5, bumps saturate. The smoother behavior of large earthquakes is due to the fact that the shaking at each specific point is the result of the integration of the contributions of the slip over the entire fracture surface. Such integration acts as a sort of low-pass filter that smoothes the average variations at short distances. Thereby the effect of attenuation (geometrical spreading) overpowers the influence of different strong parts of the fault. For magnitudes smaller than 5.0, fault lengths are not long enough to produce a large bump (the closer to the fault a station is, the more it is influenced mainly by seismic radiation from the closest part of the fault).

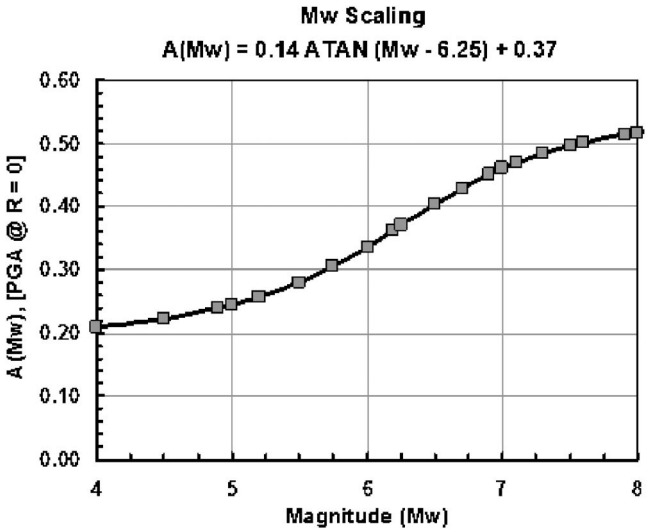

Figure 6. Magnitude scaling for strike-slip earthquakes.

MAGNITUDE AND FAULT-STYLE SCALING

In the initial stage of analysis, variations in site conditions were not distinguished. This stage is essential to obtain the main tendencies in the attenuation of ground motion. Based on the findings, the following scaling function, $A(M,F)$, is proposed:

$$A(M,F) = [c_1 \arctan(M + c_2) + c_3]F \tag{9}$$

where c_1, c_2, and c_3 are the estimator coefficients obtained from nonlinear regression, and F represents scaling due to style of faulting.

Figure 6 demonstrates the variation of magnitude scaling factor. This function type (*arctan*) is chosen since it reflects well the saturation of amplitudes of ground motion with increasing magnitudes. The scaling function is actually calibrated for $4.9 < M < 7.6$. It may need additional adjustment for lower magnitudes. Unfortunately, lack of recorded data constrains the calibration of this function for larger magnitude earthquakes.

In this study, style of faulting is considered to be a simple scale factor. According to the results of Sadigh et al. (1997) and Campbell and Bozorgnia (PEER 2006), reverse-fault events create ground motions approximately 28% higher than those from crustal strike-slips. Following this finding, we used $F = 1.00$ for strike and $F = 1.28$ for reverse faults. A limited number of normal fault data points (=15) in our data set did not allow us to constrain the fault parameter for this particular mechanism; therefore normal fault data points were treated in the same category as strike-slip faulting.

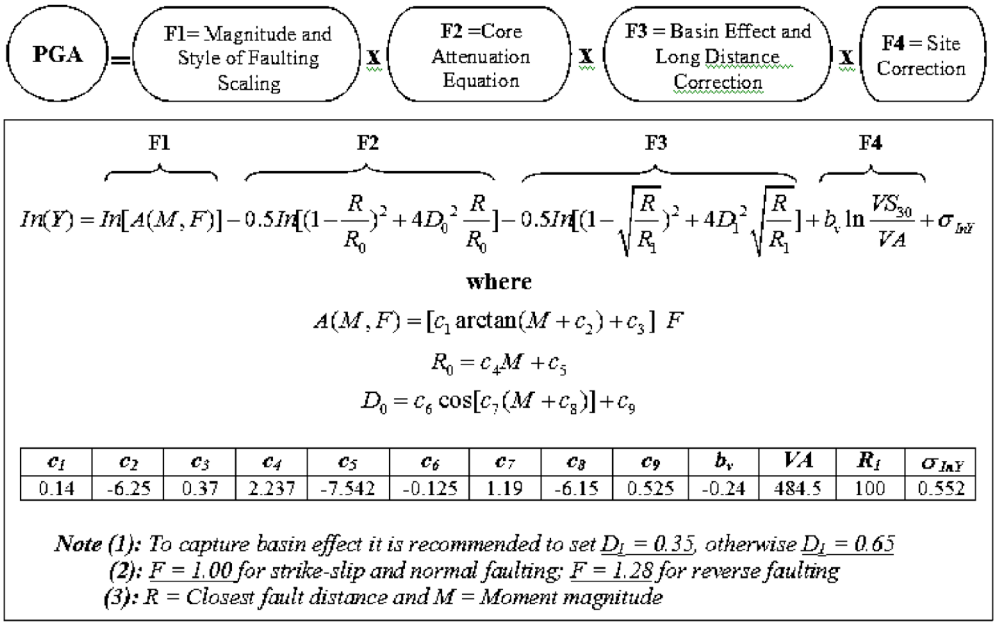

c_1	c_2	c_3	c_4	c_5	c_6	c_7	c_8	c_9	b_v	VA	R_1	σ_{lnY}
0.14	-6.25	0.37	2.237	-7.542	-0.125	1.19	-6.15	0.525	-0.24	484.5	100	0.552

Note (1): To capture basin effect it is recommended to set $D_1 = 0.35$, otherwise $D_1 = 0.65$
(2): $F = 1.00$ for strike-slip and normal faulting; $F = 1.28$ for reverse faulting
(3): R = Closest fault distance and M = Moment magnitude

Figure 7. Graizer-Kalkan ground motion attenuation model for PGA.

FINAL ATTENUATION EQUATION

Implementing three separate relationships for (i) magnitude and fault-style scaling (A), (ii) corner-distance dependence on magnitude (R_0), and (iii) damping dependence on magnitude (D_0) as given in Equations 7–9, respectively, into the core-predictive Equation 6 yields the complete attenuation model. This model is shown in Figure 7. Its estimator parameters were found through two-stage regression on a compiled data set that includes 2,583 PGA measurements. In the first stage of regression, magnitude and distance dependency on attenuation characteristics were evaluated, while in the next stage, site and basin effects (the corresponding **F3** and **F4** functions in Figure 7 are explained in detail in subsequent sections) were incorporated.

The final parameters shown in Figure 7 are valid for magnitude range of $4.5 < M < 7.6$ and a distance range up to the 200 km considered in this study. The total standard deviation (σ_{lnY}) of predictions was calculated as 0.552, which is comparable with most recent attenuation relations (PEER 2006). Residuals plots of PGA estimation for the full data set as functions of magnitude and closest distance are presented in Figure 8 together with their linear best-fit relations. With respect to both magnitude and distance, no significant trends are observed. This may serve as an evidence that magnitude and distance are independent of the total residuals.

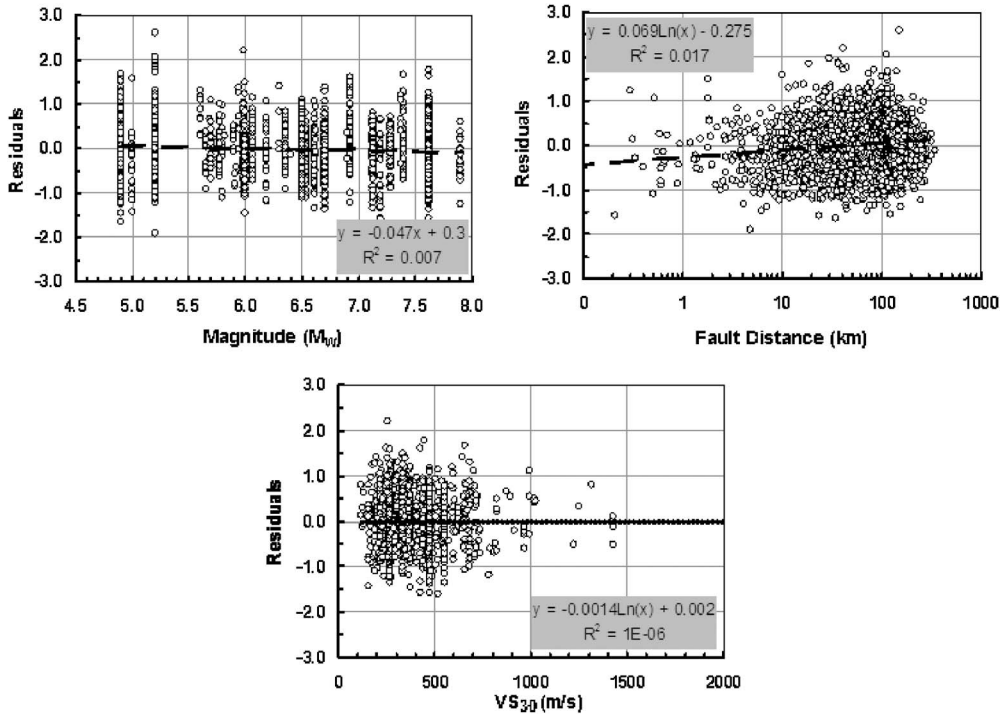

Figure 8. Distribution of residuals with respect to magnitude, closest distance, and V_{S30} measurements (dashed lines indicate the best fit for closest distance in logarithmic space, and for magnitude and V_{S30} in arithmetic space).

SHALLOW SITE CONDITIONS

Dependence of ground motion amplification on shallow site conditions has been commonly simulated in predictive equations. Some developers used linear scaling (independent from PGA) to account for amplification due to reduction in shear modulus of substrata (e.g., Boore et al. 1997). The recent attenuation models developed under NGA by Boore and Atkinson, Campbell and Bozorgnia, and Chiou and Youngs (PEER 2006) incorporated nonlinear site effects based on an empirical geotechnical model of Choi and Stewart (2005). Before making a decision on implementation of linear or nonlinear site correction, it is instructive to reflect some important findings from previous research on the observed nonlinearity in strong ground motions:

- According to Beresnev et al. (1998, 2002) and Roumelioti and Beresnev (2003), nonlinearity in strong-motion measurements is only proven for amplitudes of ground motion higher than 0.2–0.3 g in some earthquakes (1989 Loma Prieta, 1994 Northridge, and 1999 Chi-Chi); however, effects of nonlinearity on data do not show up, for example, in records of the 1987 Whittier Narrows earthquake.

- Field (2000) has recently showed that nonlinearity is a frequency-dependent phenomenon shown to take place in the frequency band of 1.0 to 5.0 Hz (0.2 to 1.0 s). It means that nonlinearity may only be effective in the short period range, while long period waves (with periods higher than 1.0 s) are practically not affected.
- Empirical results of Choi and Stewart (2005) elucidate a large degree of nonlinearity for sites with $V_{S30} < 180$ m/s, while nonlinearity rapidly diminishes with increasing V_{S30}. To be more specific, linear site amplification starts dominating beyond V_{S30} of 300 m/s.

In light of available studies, we decided to adopt linear site amplification for the following reasons:

- Peak ground acceleration is associated with different types of seismic radiation, depending upon the distance from the fault: residual displacement, shear wave, or surface wave. Evidently, frequency at which PGA occurs may be different from the site-response frequency, and consequently, degree of nonlinearity may vary significantly.
- In the database of stations used in this study with known shear-wave velocities, less than 2% of stations have $V_{S30} < 180$ m/s. This implies that nonlinearity may affect very few strong-motion records in our database; therefore its influence (if existent) on the resultant attenuation model would be minimal.
- Although use of linear site amplification may have certain limitations for very soft soil sites with $V_{S30} < 180$ m/s, compared to complex formulations of nonlinear site correction expressions (e.g., Choi and Stewart 2005), using inadequately constrained nonlinear site amplification for PGA would result in unnecessary complication on the attenuation model.

Linear site correction (i.e., linear best fit to residuals after the first step of regression) can be formulated in natural logarithmic space as:

$$F_{site} = a \ln(V_{S30}) + b \tag{10}$$

which is the equivalent form of linear site correction expression provided by Boore et al. (1997) as:

$$F_{site} = b_v \ln\left(\frac{V_{S30}}{V_A}\right) \tag{11}$$

where b_v in Equation 11 is similar to a in Equation 10, and V_A is equal to $\exp(-b/a)$. In the linear site amplification formula suggested by Boore et al., $b_v = -0.371$ and $V_A = 1{,}390$, whereas our estimates yield $b_v = -0.24$ and $V_A = 484.5$. Figure 9 compares our site correction variation with that of Boore et al. for a range of V_{S30} values. In order to compare site correction curves in a consistent manner, they were normalized by their site amplification parameters computed at $V_{S30} = 760$ m/s. As seen, our site correction factor demonstrates lower dependency on the V_{S30}. This means that our attenuation model exhibits less amplification as the V_{S30} decreases compared to stiff site conditions.

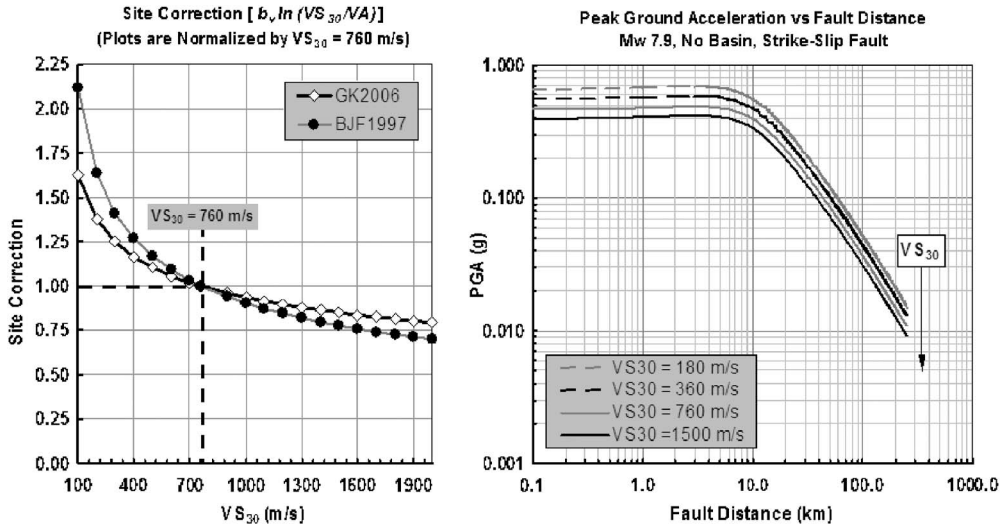

Figure 9. Comparison of normalized site correction variation with respect to V_{S30} (left); plots of PGA attenuation characteristics for various shear-wave velocities (right).

The influence of Equation 11 on the resultant attenuation curves for soil and rock sites (V_{S30}=360 and 760 m/s, respectively) are demonstrated in Figure 10 for a range of magnitude levels ($4.5 \leqslant M \leqslant 7.5$). Since the linear site correction is implemented, basically left and right panels in Figure 10 exhibit similar shapes except for shift in higher PGA values in case of lower V_{S30}.

Also compared in this figure are the attenuation plots computed for two different fault mechanisms, namely, strike-slip and reverse. Note that the difference associated with the faulting mechanism in attenuation plots is constant along the distance, which is described by a simple amplifier of F=1.28 in case of reverse faults (see amplification function $A(M,F)$ in Figure 7).

SEDIMENT-DEPTH BASIN EFFECT

There is still no consensus in either seismology or engineering communities on accounting for the site response effect in attenuation modeling. Different researchers consider certain parameters related to the site characteristics to be the most influential. The two different points of views are summarized in the following:

1. Knowledge of the average shear-wave velocity in the top 30 m below ground surface is enough to account for the site response effect (Boore et al. 1997, Boore and Atkinson [PEER 2006]).
2. The average shear-wave velocity in the top 30 m is not a significant parameter affecting the peak amplitudes. The depth of sediments is the most significant factor (Lee et al. 1995).

After examining strong-motion data recorded in different regions of California, it is

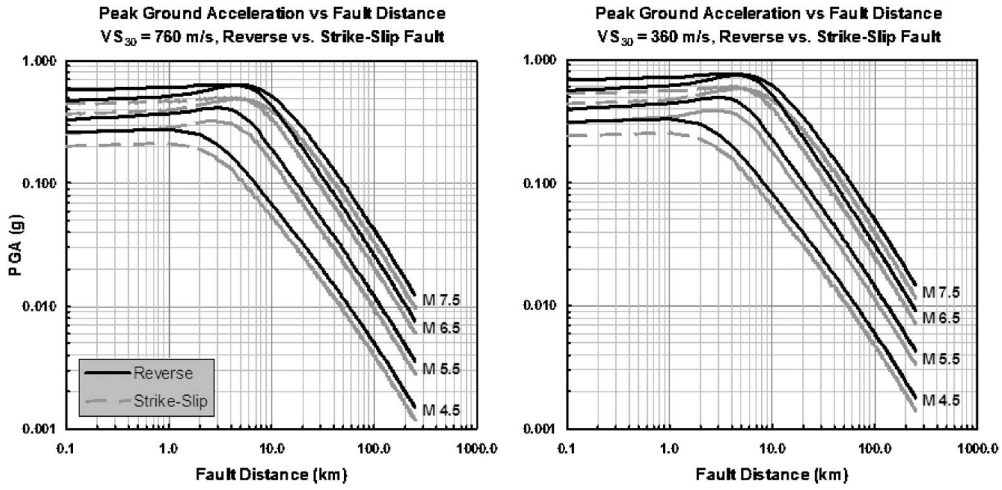

Figure 10. Comparison of PGA attenuation characteristics of proposed model for two different site categories and faulting mechanisms (note: basin effect is not included for V_{S30}=360 m/s).

concluded that both opinions may be correct if applied to limited data sets. Basically, most of the Northern California strong-motion data can be relatively well constrained by using V_{S30} without any additional information about the thickness of sediment layers. On the other hand, Southern California ground motion data are significantly influenced by basin effect (e.g., Imperial Valley, Los Angeles, and San Bernadino basins). For example, during the Hector Mine earthquake, average PGA had almost no attenuation at the distances of 130–230 km from the fault due to dominant basin effects (Graizer et al. 2002). Frankel et al. (2001) present a very convincing example of significance of basin surface waves recorded at Santa Clara Valley during a number of earthquakes. Based on our own experience as well as studies described in Field (2000), Joyner (2000), and Frankel et al. (2001), we conclude that it is necessary to account for both effects (shallow site conditions and sediment depth), and separately implement them in the attenuation model.

Basin effect significantly impacts wave field at distances of 30–50 km or more when deep sedimentary basin is present. In most cases it is associated with large-amplitude surface waves. We decided to model this effect by applying a second filter. Similar to the first filter, the transfer function of the second filter is determined by the two parameters: distance R_1 and damping D_1. In this case, R_1 describes the area of bump, and D_1 describes its amplitude (low damping D_1 produces higher amplitudes of bump; see **F3** in Figure 7).

If sediment thickness is low, basin effect can be neglected, and D_1 in this case can be taken as 0.65–0.70 (no bump). Application of the second filter with this value of D_1 results in a change of slope at distances larger than R_1 only. Attenuation function will decay proportionally to $R^{-1.5}$ (unlike R^{-1} decay produced by the first filter).

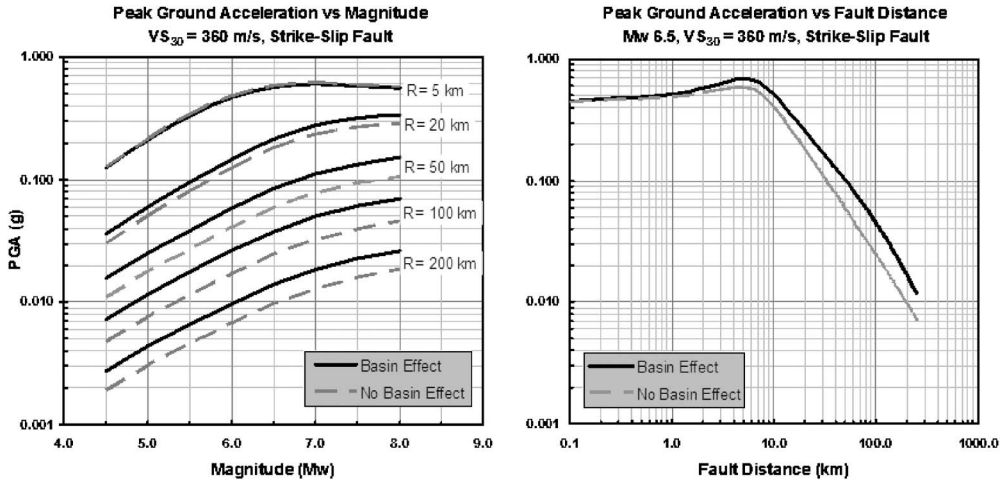

Figure 11. Comparison of magnitude scaling (left) and PGA attenuation (right) characteristics of proposed attenuation model with and without basin effects.

If basin effect is significant, D_1 can be taken as 0.3–0.4 (lower damping produces higher bump), and amplification will be applied to ground motion for distances more than about 20–30 km. At distances significantly larger than R_1, the second filter will produce the same effect as described above for higher damping: slope of resultant $(G \times G_1)$ attenuation function will change from R^{-1} to $R^{-1.5}$. In this case the resultant curve will be higher than in a no-bump case (i.e., $D_1 = 0.65 - 0.70$; see Figure 11).

In general, we envision damping parameter of the second filter (D_1) to be a smooth function of basin depth (thickness of sediment layer). But in our first approximation, we made a simplifying assumption, considering basin effect to be the same for all depths of sediments (Z) more than 1 km.

$$D_1 = \begin{cases} 0.65 & \text{for } Z < 1 \text{ km} \\ 0.35 & \text{for } Z \geqslant 1 \text{ km} \end{cases} \tag{12}$$

Following this parameterization, the influence of basin effect is demonstrated in Figure 11. In general, we expect D_1 to be decreasing smoothly from 0.7 to 0.3–0.4 and saturating with the increase of thickness of sediments (we plan to study this effect later).

The near-field ground motion attenuation is defined by one filter with D_0 and R_0. Damping D_0 describes level of amplification (bump) in the near field. The first filter describes the behavior of the attenuation function up to a distance of about 50 km, and is mostly constrained by earthquake source (magnitude in first approximation). The second filter modifies the behavior of the attenuation function according to the wave-propagation path. It reflects the influence of relatively large-scale sediment effects on the attenuation function.

The three-dimensional attenuation dependence without consideration of basin effect

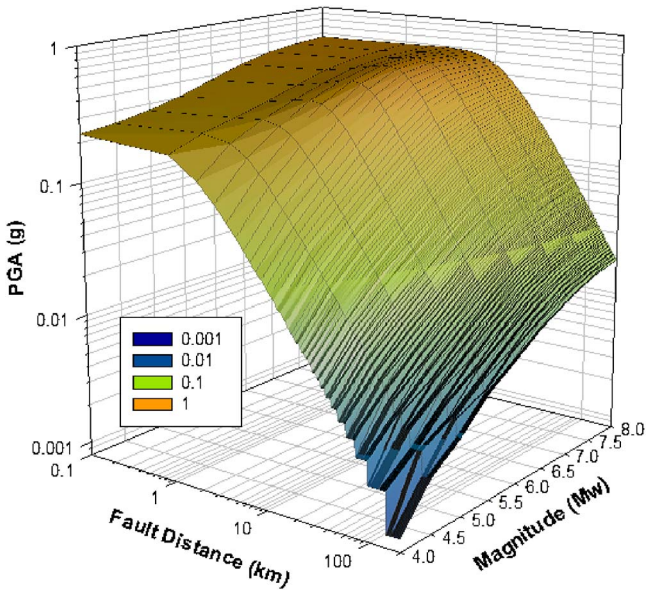

Figure 12. Three-dimensional attenuation surface for earthquakes with strike-slip faulting mechanism (V_{S30}= 360 m/s; no basin effect; note: color/shading code indicates amplitude of PGA).

is plotted for a range of magnitudes in Figure 12. This figure demonstrates the three-dimensional (PGA vs. fault distance and magnitude) attenuation surface for the strike-slip fault and provides a greater insight by freeing the magnitude term. Initiation of the bump in attenuation formulation for certain magnitudes ($M_w > 5.0$) and its subsequent disappearance for $M_w > 7.5$ can be clearly seen in this three-dimensional view.

COMPARISON WITH RECORDED DATA AND CURRENT ATTENUATION RELATIONSHIPS

Prior to comparisons with current attenuation relationships, performance of the proposed attenuation model (given in Figure 7) is examined through comparisons with actual recorded data. Figures 13 and 14 display comparisons of our predictions with one-to-one correspondence to the actual recorded PGA data from 12 earthquakes covering a magnitude range of 4.9 to 7.9. In these plots, individual site classification (in terms of V_{S30}) of each station is considered in the comparisons without necessitating grouping or averaging. This means that for each data point, there is a corresponding prediction using the exact V_{S30} of the station. For those stations without V_{S30} data available, we use V_A instead, which deactivates the site correction by turning **F4** to unity (see **F4** in Figure 7). Figures 13 and 14 collectively indicate that our predictions are strongly consistent with the recorded PGA both in the near field and far field. These plots serve as evidence not only of the stability but also the reliability of the proposed model for a range of mag-

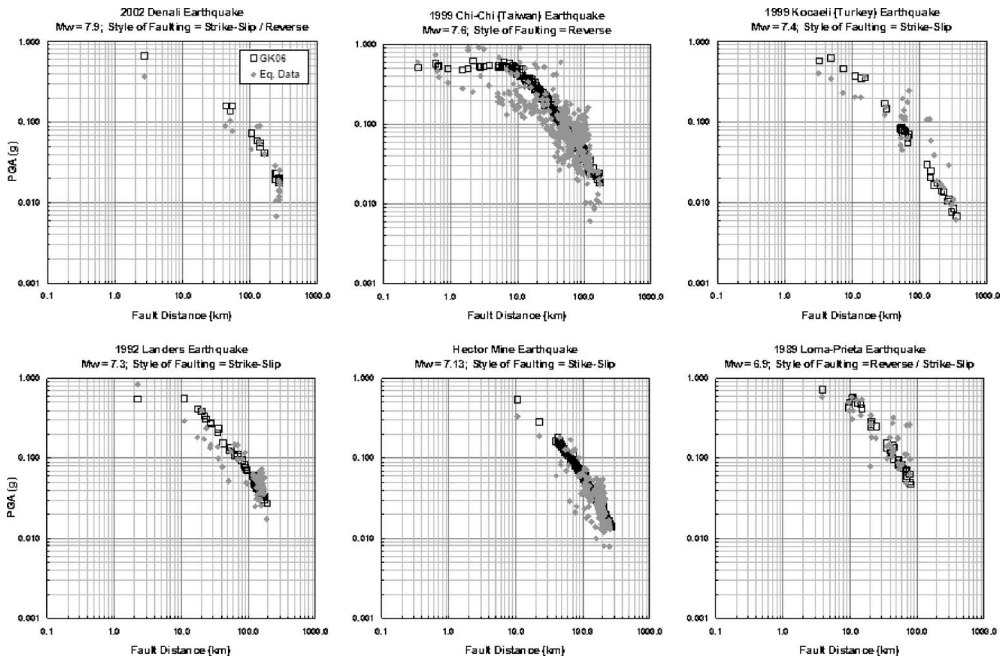

Figure 13. Event-based one-to-one comparison of actual recorded data with our predictions (M_W ranges from 6.9 to 7.9).

nitude levels. There is neither noticeable overestimation nor under-prediction of recorded data despite the diversity of data points in terms of different faulting mechanisms, site classifications, basin effects, and regional variations.

Performance of the attenuation model in predicting the recorded data is next tested against the four commonly used attenuation relationships of Abrahamson and Silva (1997), Boore et al. (1997), Campbell (1997), and Sadigh et al. (1997). These comparisons are plotted in Figures 15 and 16 using the same events shown previously in Figures 13 and 14. Besides apparent differences in the attenuation shapes, the most significant difference is evident at the area around corner distances (at the distances of between about 3 and 15 km depending upon magnitude), where our attenuation prediction yields larger acceleration values (for instance, see Parkfield 2004, Shakal et al. 2005).

Comparisons with the actual PGA data show that our attenuation curves produce good predictions compared to others, at least for Chi-Chi (M7.6), Northridge (M6.7), Imperial Valley (M6.5), and Parkfield (M6.0) earthquakes. Unfortunately, the M7.9 Denali strong-motion data set is relatively small and only includes a single record from a distance of less than 10 km. Therefore the data set of this event does not allow any conclusive decision on comparisons.

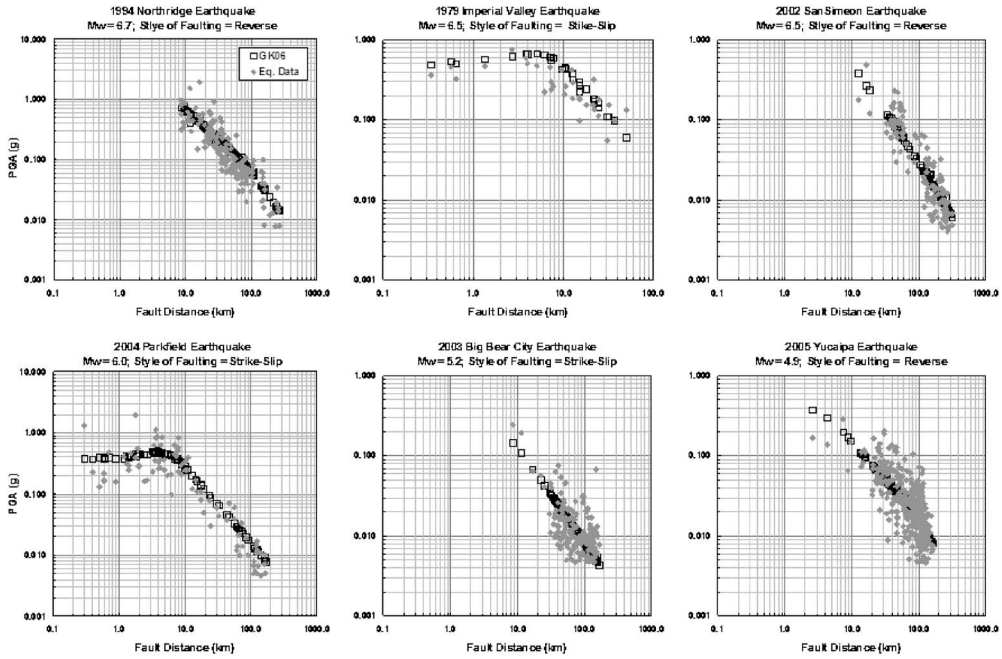

Figure 14. Event-based one-to-one comparison of actual recorded data with our predictions (M_W ranges from 4.9 to 6.7).

LARGE-DISTANCE LOW-AMPLITUDE GROUND MOTION DATA

The primary goal of this study is to develop for engineering applications an attenuation relationship for strong-motion data that have a certain distance and intensity threshold. However, it is worth mentioning that our versatile approach can also be easily applied for distant data (historically of interest in regional seismology). For a number of recent earthquakes, researchers have made an effort to combine classical strong-motion data sets (with triggered instruments) with data from seismological stations with continuous registration (e.g., Boatwright et al. 2003). Data from California earthquakes (e.g., Parkfield and San Simeon) recorded at distant stations with amplitudes of ground acceleration less than 0.005 g (typical triggering level of strong-motion instruments) demonstrate much faster attenuation with significant change of slope at large distances of more than 150–200 km from fault rupture (Figure 17). Much faster attenuation of PGA (of the order of R^{-3}) at large distances still requires physical interpretation. Nevertheless, the approach presented herein (through connecting a series of filters) is capable of capturing this long-distance fast-attenuation phenomenon by implementing another distance-dependent filter. Figure 17 demonstrate the predictive power of the attenuation curve with an additional filter against the long-distance PGA data retrieved during the Parkfield earthquake.

It is important to underscore that this additional filter does not affect attenuation at

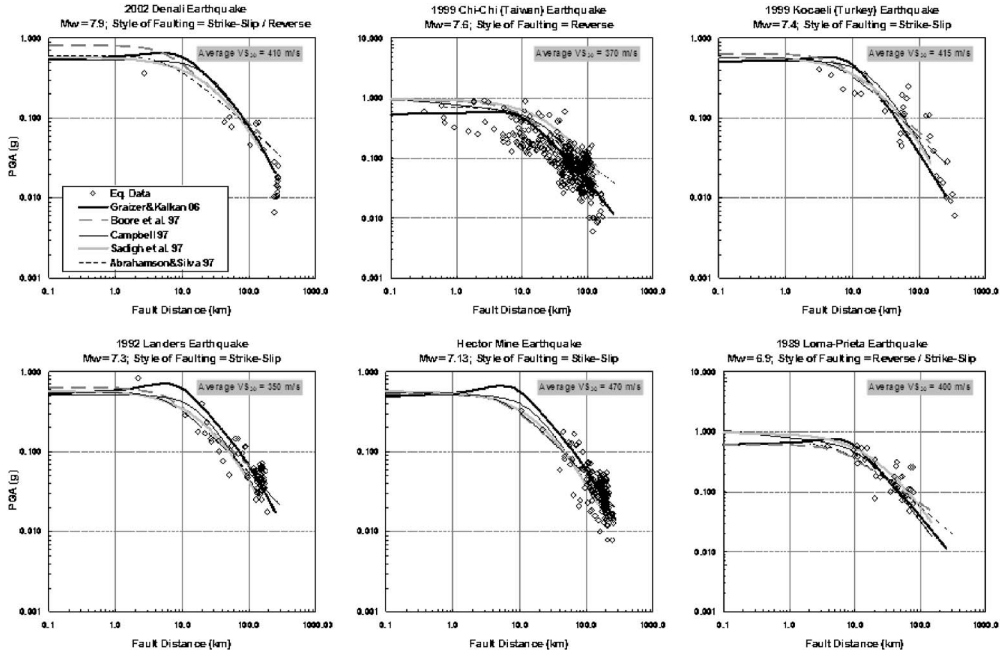

Figure 15. Event-based comparison of our predictions with those of recent attenuation relationships (M_w ranges from 6.9 to 7.9).

distances less than 150–200 km, and hence does not require reassessment of estimator coefficients computed for the core attenuation equation (as given in Figure 7). It is a unique feature of the developed model that allows further modifications to be possible without interfering with the initial settings of other filters, each designed to capture the certain behavior of seismic radiation from the fault rupture. Therefore, change in attenuation behavior at large distances can be simply ignored for engineering applications. Assuming reliability of these low-amplitude data, matching them by using existing attenuation formulas (Abrahamson and Silva 1997, Boore et al. 1997, Campbell 1997, Sadigh et al. 1997, Campbell and Bozorgnia 2003, PEER 2006) presents a real challenge.

CONCLUSIONS

In this paper, a different perspective to ground motion prediction modeling is presented. The proposed attenuation model to predict PGA is structured similarly to the transfer function of a SDOF oscillator where distance (R) serves as an equivalent of the square of frequency (f^2). A functional form of the model is composed of a series of filters, each representing a certain physical effect on the attenuation characteristics of seismic radiation. Accordingly, the first filter constituting the core equation of the attenuation relationship has a response characteristic with a constant level at very short fault distances, a bump or a turning point around corner distance R_0 (depending on magnitude), and a decrease proportional to R^{-1}. The second filter has a constant level till R_1

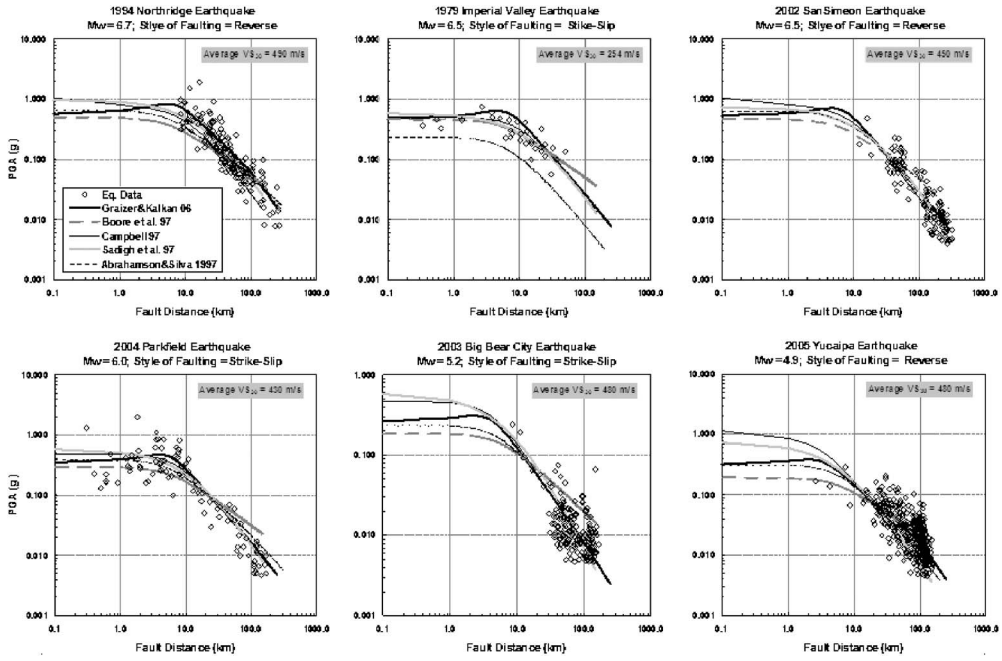

Figure 16. Event-based comparison of our predictions with those of recent attenuation relationships (M_w ranges from 4.9 to 6.7).

(around 100 km from the fault), damping $D_1=0.65$ (no amplification), and a decrease proportional to $R^{-0.5}$. Introducing a second filter with these settings does not essentially affect attenuation of PGA at distances shorter than R_1, and results in faster attenuation in the order of $R^{-1.5}$ at distances more than R_1. If parameterized accordingly (e.g., $R_1=100$ km and $D_1=0.35$), this secondary filter can effectively capture basin effect by slightly amplifying ground motions in the near field and more at distances around and larger than R_1. These settings also result in faster attenuation $R^{-1.5}$ at distances more than threshold distance R_1. The attenuation-model coefficients were derived using a large set of ground motion data (2,583 data points). We utilized 33 main shock data sets from the NGA database. Further, records from main shocks of 14 earthquakes from California, Turkey, and the former USSR were also included in the regression.

The developed attenuation relationship considers scaling due to magnitude, style of faulting, site amplification, and basin effects. We adapted linear site amplification expression based on V_{S30} classification to correct for the site effect (similar to Boore et al. [1997], but with lower dependency on V_{S30}). We also applied basin-effect correction by changing the D_1 parameter in the second filter to account for deep sedimentary site response. The present model for crustal reverse-fault events predicts ground motions about 28% higher than those from strike-slip and normal-fault events.

None of the existing attenuations allows PGA to reach its maximum value at some

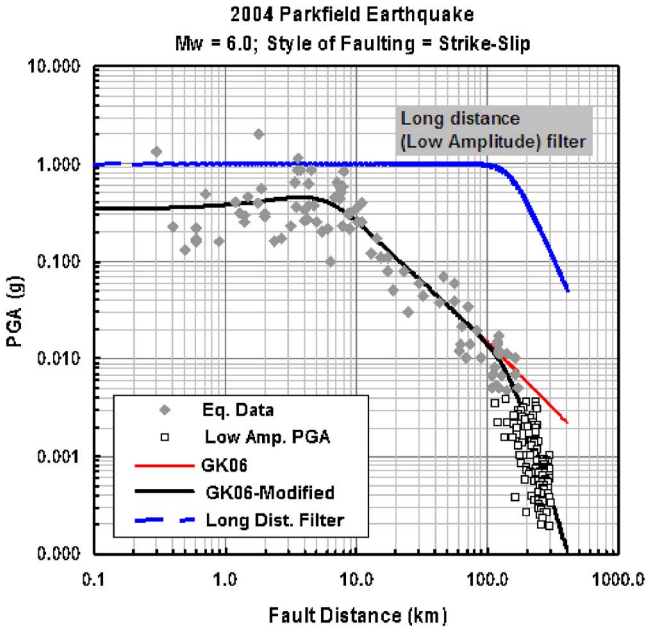

Figure 17. Implementation of long-distance filter to capture low-amplitude PGA attenuation characteristics.

distance from the fault. However, the proposed attenuation relationship can effectively capture this phenomenon, observed in a number of events. Compared to actual strong-motion data, the proposed model yields consistently good predictions not only in the near-fault region but also at farther distances for a broad range of magnitude levels. The total standard error (σ_{lnY}) of 0.552 is comparable to other attenuation models. Residual analyses show that distributions of total residuals with respect to distance and magnitude are not biased.

The architecture of the proposed ground motion attenuation model is extremely versatile because it makes possible further modifications and refinements through the implementation of additional filters to the existing filter series. These additional filters can be designed in such a way that they only affect distances more than R_n without influencing characteristic (i.e., parameters) of attenuation at shorter distances. This essentially allows expanding attenuation relationships, for farther distances without changing behavior at shorter distances.

The presented approach to ground motion attenuation modeling can potentially be used for earthquakes in other seismotectonic regions with subduction and intra-plate events. We are also planning on expanding the current relation to predict spectral accelerations and peak ground velocity.

ACKNOWLEDGMENTS

The authors are grateful to the Pacific Earthquake Engineering Research Center for making the Next Generation Attenuation Relationships (NGA) project database available. Sincere thanks are extended to M. Reichle, M. Trifunac, A. Frankel, P. Malhotra, B. Darragh, I. Beresnev, and three anonymous reviewers for their valuable comments and suggestions, which improved the technical quality of the paper. Any opinions, findings, and conclusions or recommendations expressed in this material are those of the authors solely and do not reflect the views of the California Geological Survey.

REFERENCES

Abrahamson, N. A., and Silva, W. J., 1997. Empirical response spectral attenuation relations for shallow crustal earthquakes, *Seismol. Res. Lett.* **68**, 94–127.

Beresnev, I. A., 2002. Nonlinearity at California generic soil sites from modeling recent strong-motion data, *Bull. Seismol. Soc. Am.* **92**, 863–870.

Beresnev, I. A., Field, E. H., Van Den Abeele, K., and Johnson, P. A., 1998. Magnitude of nonlinear sediment response in Los Angeles basin during the 1994 Northridge, California, earthquake, *Bull. Seismol. Soc. Am.* **88**, 1079–1084.

Boatwright, J., Bundock, H., Luetgert, J., Seekins, L., Gee, L., and Lombard, P., 2003. The dependence of PGA and PGV on distance and magnitude inferred from Northern California ShakeMap data, *Bull. Seismol. Soc. Am.* **93**, 2043–2055.

Boore, D. M., Joyner, W. B., and Fumal, T. E., 1997. Equations for estimating horizontal response spectra and peak acceleration from western North American earthquakes: a summary of recent work, *Seismol. Res. Lett.* **68**, 128–153.

Brune, J., 1970. Tectonic stress and the spectra of seismic shear waves from earthquakes, *J. Geophys. Res.* **75**, 4997–5009.

——, 1971. Correction, *J. Geophys. Res.* **76**, 5002.

Campbell, K. W., 1997. Empirical near-source attenuation relationships for horizontal and vertical components of peak ground acceleration, peak ground velocity, and pseudo-absolute acceleration response spectra, *Seismol. Res. Lett.* **68**, 154–179.

——, 2003. Strong-motion attenuation relations, in *International Handbook of Earthquake and Engineering Seismology, Part B*, edited by W. H. K. Lee, H. Kanamori, P. C. Jennings, and C. Kisslinger, Academic Press, Burlington, Mass., pp. 1003–1012.

Campbell, K. W., and Bozorgnia, Y., 2003. Updated near-source ground motion (attenuation) relations for the horizontal and vertical components of peak ground acceleration and acceleration response spectra, *Bull. Seismol. Soc. Am.* **93**, 314–331.

Chinnery, M. A., 1961. The deformation of the ground around surface faults, *Bull. Seismol. Soc. Am.* **51**, 355–372.

Choi, Y., and Stewart, J. P., 2005. Nonlinear site amplification as a function of 30 m shear wave velocity, *Earthquake Spectra* **21**, 1–30.

Field, E. H., ed., 2000. Accounting for site effects in probabilistic hazard analyses in Southern California, *Bull. Seismol. Soc. Am.* **90**, 244.

Frankel, A., 1995. Simulating strong motions of large earthquakes using recordings of small

earthquakes: the Loma Prieta Mainshock as a test case, *Bull. Seismol. Soc. Am.* **85**, 1144–1160.

Frankel, A., Carver, D., Cranswick, E., Bice, T., Sell, R., and Hanson, S., 2001. Observation of basin ground motions from a dense seismic array in San Jose, California, *Bull. Seismol. Soc. Am.* **91**, 1–12.

Graizer, V., Shakal, A., Scrivner, C., Hauksson, E., Polet, J., and Jones, L., 2002. TriNet strong-motion data from the M7.1 Hector Mine, California, earthquake of 16 October 1999, *Bull. Seismol. Soc. Am.* **92**, 1525–1541.

Haskell, N. A., 1969. Elastic displacements in the near-field of a propagating fault, *Bull. Seismol. Soc. Am.* **59**, 865–908.

Joyner, W. B., 2000. Strong motion from surface waves in deep sedimentary basins, *Bull. Seismol. Soc. Am.* **90**, S95–S112.

Kalkan, E., and Gülkan, P., 2004. Site-dependent spectra derived from ground motion records in Turkey, *Earthquake Spectra* **20**, 1111–1138.

Lee, V. W., Trifunac, M. D., Todorovska, M. I., and Novikova, E. I., 1995. *Empirical Equations Describing Attenuation of Peak of Strong Ground Motion, in Terms of Magnitude, Distance, Path Effects and Site Conditions, Report No. CE 95-02*, University of Southern California, Los Angeles.

Pacific Earthquake Engineering Research Center (PEER), 2006. *Interim Reports of Next Generation Attenuation (NGA) Models, July 2006*, PEER, University of California, Berkeley [available at: http://peer.berkeley.edu/lifelines/repngamodels.html].

Power, M., Chiou, B., Abrahamson, N., and Roblee, C., 2006. The next generation of ground motion attenuation models, (NGA) project: an overview, *Proceedings, Eighth National Conference on Earthquake Engineering*, Paper No. 2022.

Roumelioti, Z., and Beresnev, I. A., 2003. Stochastic finite-fault modeling of ground motions from the 1999 Chi-Chi, Taiwan, earthquake: application to rock and soil sites with implications for nonlinear site response, *Bull. Seismol. Soc. Am.* **93**, 1691–1702.

Sadigh, K., Chang, C.-Y., Egan, J. A., Makdisi, F., and Youngs, R. R., 1997. Attenuation relationships for shallow crustal earthquakes based on California strong motion data, *Seismol. Res. Lett.* **68**, 180–189.

Shakal, A., Graizer, V., Huang, M., Borchardt, R., Haddadi, H., Lin, K., Stephens, K., and Roffers, P., 2005. Preliminary analysis of strong-motion recordings from the 28 September 2004 Parkfield, California earthquake, *Seismol. Res. Lett.* **76**, 27–39.

Somerville, P. G., and Yoshimura, J., 1990. The influences of critical Moho reflections on strong ground motion recorded in San Francisco and Oakland during the 1989 Loma Prieta earthquake, *Geophys. Res. Lett.* **17**, 1203–1206.

Trifunac, M. D., 1976. Preliminary analysis of the peaks of strong earthquake ground motion—dependence of peaks on earthquake magnitude, epicentral distance, and recording site conditions, *Bull. Seismol. Soc. Am.* **66**, 189–219.

(Received 10 August 2006; accepted 22 January 2007)